Astronomy & Astrophysics manuscript no. yjc16
November 22, 2016
©ESO 2016

Concentrating small particles in protoplanetary disks through the streaming instability

C.-C. Yang (楊朝欽), A. Johansen, and D. Carrera

Lund Observatory, Department of Astronomy and Theoretical Physics, Lund University, Box 43, SE-221 00 Lund, Sweden
e-mail: ccyang@astro.lu.se

November 22, 2016

arXiv:1611.07014v1 [astro-ph.EP] 21 Nov 2016

ABSTRACT

Laboratory experiments indicate that direct growth of silicate grains via mutual collisions can only produce particles up to roughly millimeters in size. On the other hand, recent simulations of the streaming instability have shown that mm/cm-sized particles require an excessively high metallicity for dense filaments to emerge. Using the numerical algorithm of Yang & Johansen (2016) for stiff mutual drag force, we revisit the investigations of Carrera et al. (2015) and perform simulations of small particles with significantly higher resolutions and longer simulation times. We find that particles of dimensionless stopping time $\tau_s = 10^{-2}$ and 10^{-3} – representing mm- and cm-sized particles interior of the water ice line – concentrate themselves via the streaming instability at a solid abundance of a few percent. We thus revise the critical solid abundance curve of Carrera et al. (2015) for the regime of $\tau_s \ll 1$. The solid density in the concentrated regions reaches values higher than the Roche density, indicating that gravitational contraction into planetesimals is possible. Our results hence bridge the gap in particle size between direct dust growth limited by bouncing and the streaming instability.

Key words. hydrodynamics – instabilities – methods: numerical – minor planets, asteroids: general – planets and satellites: formation – protoplanetary disks

1. Introduction

In the core-accretion scenario of planet formation, planetary cores are assembled beginning with interstellar μm-sized dust grains (Safronov 1969). This process of growing planetary cores covers more than 30 orders of magnitude in mass and more than 13 orders of magnitude in size, required to be completed within the 1–5 Myr lifetime of their natal protoplanetary disks (e.g., Haisch et al. 2001; Mamajek 2009). The course of planet formation is usually divided into different stages according to the size of the solids or planetary objects involved, and each stage has its own major difficulties (e.g., Papaloizou & Terquem 2006; Baruteau et al. 2014; Testi et al. 2014). One of these stages yet to be understood is the formation of kilometer-scale planetesimals (see, e.g., Johansen et al. 2014, and references therein).

One major obstacle to the formation of planetesimals is the "radial-drift barrier." Solid particles marginally coupled to the gas via drag force drift radially inwards and are quickly removed from protoplanetary disks due to constant head wind (Adachi et al. 1976; Weidenschilling 1977a). For example, the timescale for the radial drift of meter-sized boulders at ∼1 au of the minimum mass solar nebula (MMSN; Weidenschilling 1977b; Hayashi 1981) is ∼100 yr, significantly shorter than the typical lifetime of the disks. In fact, solid particles of a wide range of sizes at various locations in disks suffer from the radial drift (e.g., Brauer et al. 2007; Youdin 2010). To circumvent this barrier, some mechanism(s) to efficiently concentrate solid materials into high density so that direct gravitational collapse can occur is required.[1]

Two types of mechanisms to concentrate solid materials exist: one is passive, and the other is active. The former includes long-lived local pressure maxima (Whipple 1972; Johansen et al. 2009a; Bai & Stone 2014) or vortices (Barge & Sommeria 1995; Klahr & Hubbard 2014; Lyra 2014), in which solids passively follow the underlying flow of gas by friction. By contrast, the streaming instability discovered by Youdin & Goodman (2005) is realized by the action-reaction pair of the drag force between solid particles and gas, with which the solids actively engage in the dynamics with the gas to spontaneously concentrate themselves into high densities (Johansen & Youdin 2007; Bai & Stone 2010a; Yang & Johansen 2014). As a result, not only the dense filamentary structure of solids driven by the streaming instability has significantly reduced radial drift speeds, but also planetesimals can form by direct gravitational collapse within these dense filaments (Johansen et al. 2012, 2015; Simon et al. 2016; Schäfer et al. 2016).

However, it remains problematic for the streaming instability to drive planetesimal formation inside the ice line of protoplanetary disks (Drążkowska & Dullemond 2014). Direct dust growth by coagulation of silicate grains is limited to mm sizes, due to bouncing and fragmentation at collisions (Zsom et al. 2010; Birnstiel et al. 2012). On the other hand, there exists a threshold in solid abundance only above which the streaming instability can drive solid concentration into high densities (Johansen et al. 2009b; Bai & Stone 2010a). Using a suite of two-dimensional simulations, Carrera et al. (2015) found that this threshold abundance increases drastically with decreasing particle size. For mm-sized particles inside the ice line of protoplanetary disks, they suggested that a solid-to-gas column density ratio of more than 10% is required, an exceedingly high value in usual disk conditions. Therefore, it seems that a significant gap

[1] Yet another possibility is to keep the friction time short by aggregating porous icy dust during its growth (Kataoka et al. 2013). This process, however, may only operate outside the ice line.

between dust coagulation and the onset of planetesimal formation exists inside the ice line of young protoplanetary disks.

A few properties of the streaming instability are worth noticing, though, which may explain the exceedingly high critical solid abundance found for small particles. First, even though the growth rate of the linear streaming instability for small particles is relatively small compared to that for large particles when the local solid-to-gas density ratio is low, it significantly overtakes that for large particles when the density ratio is more than the order of unity (Youdin & Johansen 2007). Hence, the response of small particles to the streaming instability should be more prominent when the latter condition is reached. However, the wavelengths of the fastest growing modes are roughly proportional to the dimensionless stopping time $\tau_s \equiv \Omega_K t_s$, and thus the size of the particles, where Ω_K is the local Keplerian frequency and t_s is the stopping time characterizing the mutual drag force between the gas and the particles (Youdin & Johansen 2007). These wavelengths are as small as $\sim 10^{-4} H$ for particles with $\tau_s \sim 10^{-3}$, where H is the local scale height of the gas (Bai & Stone 2010b). Resolving these faster growing modes of the streaming instability remains challenging in current numerical simulations, and systematic resolution study towards high resolutions seems warranted. Finally, in the nonlinear stage of the streaming instability, the timescales for sedimentation and radial drift of the particles should continue to be relevant for the system. These timescales are inversely proportional to τ_s when $\tau_s \ll 1$, and hence proportionately longer time may be required for small particles to concentrate themselves than their large counterparts.

It is numerically challenging to simulate the particle-gas system in question with higher resolution and longer simulation time than was achieved by Carrera et al. (2015), due to stringent time-step constraint of the stiff mutual drag force. To make such simulations feasible, we have devised a new algorithm in Yang & Johansen (2016) to relieve this time-step constraint, and we have demonstrated that the algorithm manages small particles and/or strong local solid concentration with satisfactory numerical convergence and accuracy. Employing this technique in this work, we revisit Carrera et al. (2015) for the case of dimensionless stopping time $\tau_s \ll 1$ with significantly higher resolutions and longer simulation times.

We indeed find these small particles can spontaneously concentrate themselves into high density at a much reduced solid abundance: $\sim$1–2% for particles of $\tau_s = 10^{-2}$ while $\sim$3–4% for particles of $\tau_s = 10^{-3}$. In the next section, we briefly describe our methodology. We then present the evolution of the system, focusing on the concentration of the solid particles, in both two-dimensional (2D; Sect. 3) and three-dimensional (3D; Sect. 4) models. The implications for the formation of planetesimals are discussed in Sect. 5, where we revise the critical solid abundance of Carrera et al. (2015) with the results of this work. We conclude with a short summary in Sect. 6.

2. Methodology

As in our previous publication in Yang & Johansen (2014), we use the local-shearing-box approximation (Goldreich & Lynden-Bell 1965) to simulate a system of gas and solid particles. The computational domain is a small rectangular box at an arbitrary distance from the central star. Its origin rotates around the star at the local Keplerian angular speed Ω_K and its three axes constantly align in the radial, azimuthal, and vertical directions, respectively. We consider isothermal, non-magnetized gas in a regular Eulerian grid with numerous Lagrangian solid particles in it. The gas interacts with each of the particles via their mutual drag force, which is characterized by the stopping time t_s (Whipple 1972; Weidenschilling 1977a) or its dimensionless counterpart $\tau_s \equiv \Omega_K t_s$ (Youdin & Goodman 2005). We include the linearized vertical gravity due to the central star on the particles but ignore it for the gas, since the computational domain considered in this work is so small compared to the vertical scale height of the gas that there is no appreciable vertical density stratification in the gas over the domain.[2] For simplicity, we assume that all particles have the same stopping time.[3] We also ignore collisional effects between and self-gravity of the particles in order to isolate the effects driven by the streaming instability. The standard sheared periodic boundary conditions are imposed (Brandenburg et al. 1995; Hawley et al. 1995), and we assume the vertical dimension is also periodic.

To evolve this system of gas and particles, we use the Pencil Code[4], a high-order finite-difference simulation code for astrophysical fluids and particles (Brandenburg & Dobler 2002). It employs sixth-order centered differences for all spatial derivatives and a third-order Runge-Kutta method to integrate the system of equations. To maintain numerical stability, hyper-diffusion operators are needed in each dynamical field variable for the gas, and we fix the mesh Reynolds number for these operators so that noise close to the Nyquist frequency is properly damped while the power over large dynamical range is preserved (Yang & Krumholz 2012). Furthermore, we use a sixth-order B-spline interpolation to integrate the shear advection terms (c.f., Johansen et al. 2009a). As mentioned above, the solid particles are modeled as Lagrangian (super-)particles, which have individual positions and velocities that are integrated in unison with the Runge–Kutta steps. Their interaction with the Eulerian gas is achieved by the standard particle-mesh method (see, e.g., Hockney & Eastwood 1988). To obtain high spatial accuracy, we choose the Triangular-Shaped-Cloud scheme for the particle-mesh interpolation and assignment.

Since we focus our attention in this work on small particles with potentially strong local solid concentrations, the mutual drag force between the gas and the particles is stiff. In this regard, we employ the numerical algorithm developed in Yang & Johansen (2016) to relieve the stringent time step constraint due to this stiffness of the drag force. This algorithm intricately decomposes the globally coupled system of equations and makes it possible to integrate the equations on a cell-by-cell basis. It uses the analytical solutions in each cell to achieve numerical stability with arbitrary time step. The momentum feedback from the particles to the gas cells is also an essential ingredient to expedite numerical convergence.

For comparison purposes, we investigate both 2D (radial-vertical) and 3D models. The computational domain has a size of either $0.2H$ or $0.4H$ in each direction, where H is the vertical scale height of the gas. We consider solid particles of $\tau_s = 10^{-2}$ and $\tau_s = 10^{-3}$, which are approximately cm and mm in size (when their porosity is low) at $\sim$2.5 au in the primordial MMSN, respectively (e.g., Johansen et al. 2014). At later stages of disk evolution, these stopping times represent particles approximately 10 times smaller (Bitsch et al. 2015). An external radial pressure gradient to the gas is imposed so that the az-

[2] We have specifically checked several low-resolution models with vertical gravity on the gas in effect and do not find noticeable difference in the results.

[3] It has been suggested that the particle concentration driven by the streaming instability is predominantly determined by the largest ones for a population of particles of various sizes (Bai & Stone 2010a).

[4] The Pencil Code is publicly available at `http://pencil-code.nordita.org/`

Table 1: Model Specifications

Dimensionless Stopping Time τ_s	Solid Abundance Z	Computational Domain	Resolutions (H^{-1})	Simulation Time (P)
2D (radial-vertical) Models				
10^{-2}	0.01	$0.2H \times 0.2H$	640, 1280, 2560	4000
		$0.4H \times 0.4H$	320, 640, 1280	4000
	0.02	$0.2H \times 0.2H$	640, 1280, 2560, 5120	1000
		$0.4H \times 0.4H$	320, 640, 1280, 2560	1000
	0.04	$0.2H \times 0.2H$	640, 1280, 2560	1000
		$0.4H \times 0.4H$	320, 640, 1280	1000
10^{-3}	0.02	$0.2H \times 0.2H$	640, 1280, 2560	1000
		$0.4H \times 0.4H$	320, 640, 1280	1000
	0.03	$0.2H \times 0.2H$	640, 1280, 2560	5000
		$0.4H \times 0.4H$	320, 640, 1280	5000
	0.04	$0.2H \times 0.2H$	640, 1280, 2560	2000[a]
		$0.4H \times 0.4H$	320, 640, 1280	2000
3D Models				
10^{-2}	0.02	$0.2H \times 0.2H \times 0.2H$	160, 320, 640	1000
10^{-3}	0.04	$0.2H \times 0.2H \times 0.2H$	160, 320, 640	1000

Notes. [(a)] Except for the resolution of $2560H^{-1}$, which is up to $\sim 1650P$.

imuthal velocity of the gas is reduced by $\Delta v \equiv \Pi c_s = 0.05 c_s$, a typical value in the inner region of the MMSN, where c_s is the isothermal speed of sound (Bai & Stone 2010a; Bitsch et al. 2015).

The initial conditions are set as follows. Given that it experiences no vertical gravity, the gas has a uniform density of ρ_0. On the other hand, we allocate on average one particle per gas cell but randomly position the particles, such that the particle density distribution is vertically Gaussian with a constant scale height of $0.02H$. All the (super-)particles have the same mass, which is determined by the solid-to-gas mass ratio $Z \equiv \Sigma_{\rm p,0}/\Sigma_{\rm g,0}$, where $\Sigma_{\rm p,0}$ and $\Sigma_{\rm g,0} = \sqrt{2\pi}\rho_0 H$ are the initial uniform column densities of the particles and the gas, respectively (see Yang & Johansen 2014). With the density fields of the gas and the particles fixed, we apply the Nakagawa–Sekiya–Hayashi (1986) equilibrium solutions to the horizontal velocities of the gas and the particles. Their initial vertical velocities are set zero.

All the models we have investigated are listed in Table 1. For each set of model parameters, we evolve the system for at least $1000P$, where $P = 2\pi/\Omega_K$ is the local orbital period. This is a significantly long simulation time compared to previous works in the literature, which is necessary to capture the timescale for the streaming instability to operate on and concentrate sedimented small particles, as discussed in detail in the following sections.

3. Two-dimensional models

In this section, we discuss the evolution of the density distribution of the particle layer found in our 2D models. The system is axisymmetric in this case, with only radial and vertical variations. We divide the discussion of the models by the dimensionless stopping time τ_s of the particles.

3.1. Particles of $\tau_s = 10^{-2}$

Figure 1 shows the evolution of the particle layer from three of our 2D models with particles of $\tau_s = 10^{-2}$. They have the same computational domain of $0.2H \times 0.2H$ and resolution of $2560H^{-1}$, but differ in their solid abundance Z: $Z = 0.01$, 0.02, and 0.04.

We first compare the cases of $Z = 0.01$ and $Z = 0.02$. For $t \lesssim 100P$, both models follow similar evolution. The particles continue their sedimentation toward the mid-plane during the first $\sim 20P$, from the initial scale height of $0.02H$ down to $\sim 0.013H$ and $\sim 0.012H$ for $Z = 0.01$ and 0.02, respectively (Fig. 2). Note that the (e-folding) timescale for sedimentation is approximately $(2\pi\tau_s)^{-1}P$, which is $\sim 16P$ for particles of $\tau_s = 10^{-2}$. In the mean time, random voids of various sizes driven by the streaming instability are developed and they move around throughout the particle layer, which is the same phenomenon found in the unstratified simulations of saturated streaming turbulence of tightly-coupled particles (Johansen & Youdin 2007; Yang & Johansen 2016). After $t \sim 20P$, the particles do not sediment anymore due to their random motion. Furthermore, vertical oscillation of the particle layer starts to develop and the layer becomes increasingly more corrugated (Fig. 1). In this manner, a small but appreciable fraction of the particles can be slung away from the mid-plane and move close to the vertical boundary. As a result, the scale height of the particle layer gradually increases with time and reaches a level of $\sim 0.020H$ and $\sim 0.016H$ for $Z = 0.01$ and 0.02, respectively, when $t \sim 100P$ (Fig. 2). Similar corrugation mode was also reported by Lorén-Aguilar & Bate (2015), who suggested that it is driven by large-scale toroidal vortices. However, we have not found evidence for such large-scale vortices in the particle layer in our models, due to complicated small-scale particle flow in the streaming turbulence. Moreover, it remains unclear how boundary conditions affect this structure, which needs to be further investigated (R. Li et al. 2016, in preparation; see also the discussion on the effect of other aspects of the model below).

For $t > 100P$, the model with solid abundance $Z = 0.01$ maintains the same state up to $t = 4000P$, without any sign of further concentration of solid particles.[5] By drastic contrast, however, the model with $Z = 0.02$ shows appreciable radial concentration of solids in the mid-plane over time, as shown in Fig. 1, the left panels of Fig. 2, and Fig. 3a. A first dominant con-

[5] We only show the state up to $t = 1000P$ in Fig. 1.

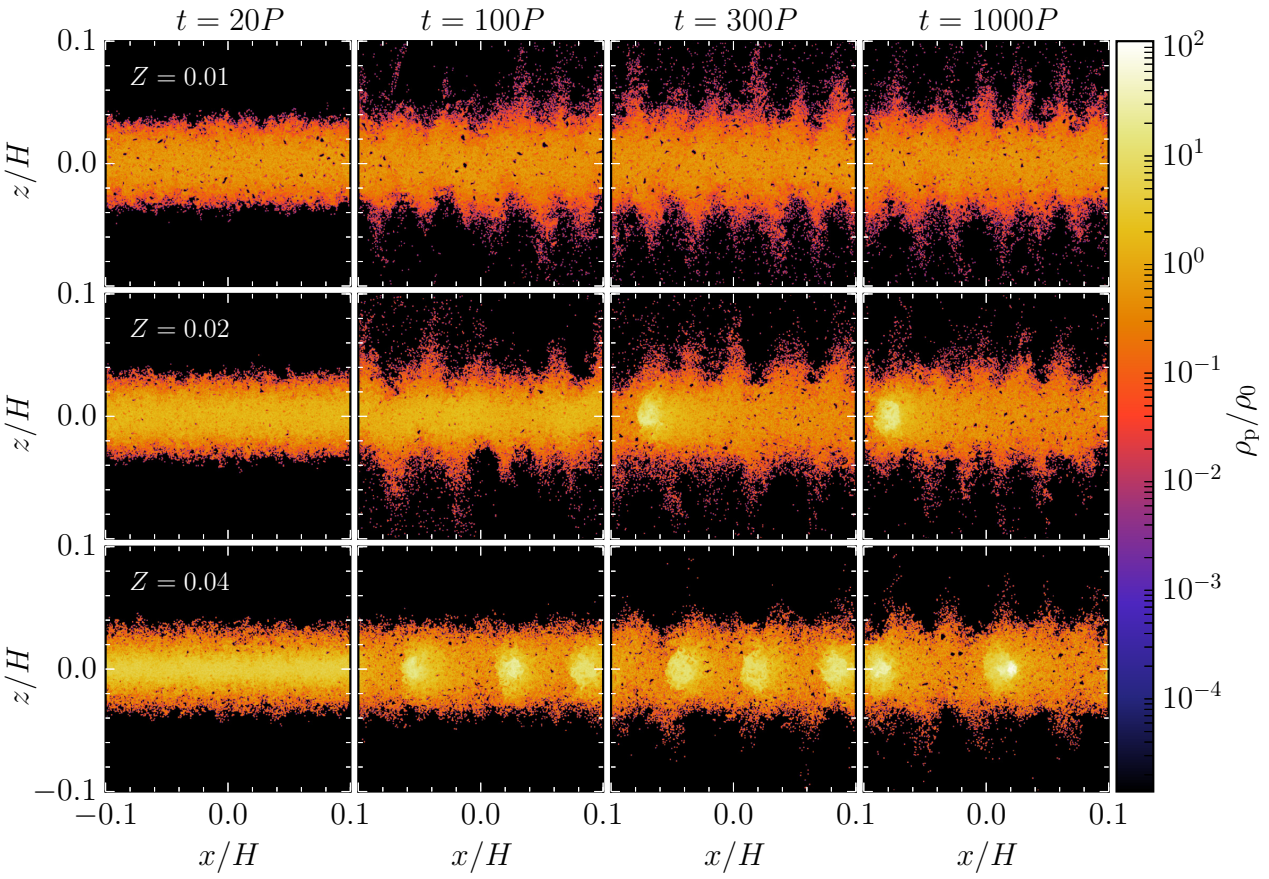

Fig. 1: Evolution of the particle density distribution for 2D models with particles of dimensionless stopping time $\tau_s = 10^{-2}$. The top, middle, and bottom panels show the models with an increasing solid abundance of $Z = 0.01$, 0.02, and 0.04, respectively, and the time t in terms of the local orbital period P increases from left to right. The particle density ρ_p is measured with respect to the initial gas density in the mid-plane ρ_0, and the radial and vertical positions are expressed in terms of the vertical scale height of the gas H. The models have a computational domain of $0.2H \times 0.2H$ and a resolution of $2560H^{-1}$.

centration begins at $t \sim 100P$ and reaches its peak at $t \sim 230P$. A second even stronger concentration closely upstream appears soon afterward while the first is dispersed. This second concentration reaches its saturation state at $t \sim 400P$ and then maintains its dominance and equilibrium up to the end of the simulation ($t = 1000P$). At this state, the solid concentration attains a peak local density of ~30 times the background gas density (Fig. 2).

The left panels of Fig. 2 shows the evolution of the scale height and maximum local density of the particle layer for all of our 2D models with dimensionless stopping time $\tau_s = 10^{-2}$ and solid abundance $Z = 0.02$. For the first ~$50P$, during which the streaming turbulence is established, it is seen that the higher the resolution, the earlier the establishment and the larger the local maximum density of solids result. This is consistent with the fact that more and more faster growing modes of the linear streaming instability as well as smaller-scale structures in the particle layer are resolved (Youdin & Goodman 2005; Youdin & Johansen 2007). We note that even at our highest resolution, $5120H^{-1}$, the fastest growing mode of the linear streaming instability remains well under-resolved, the wavelength of which is on the order of $10^{-4}H$ (c.f., Bai & Stone 2010b; Yang & Johansen 2016). It is also seen that the higher the resolution, the higher the scale height of the particle layer is in this initial stage. On the other hand, the timescale to establish the corrugation of the particle layer does not seem to depend on resolution, but sensitively on computational domain. As shown in Fig. 2, these timescales for our $0.2H \times 0.2H$ and $0.4H \times 0.4H$ models are ~$100P$ and ~$400P$, respectively. Nevertheless, the degree of the vertical excitation of the particle layer is rather similar between the two computational domains and between different resolutions.

The corresponding time averages of the properties shown in Fig. 2 at the saturation state are summarized in Table 2. There exists some critical model resolution above which significantly stronger solid concentration occurs; this critical resolution is around 512 grid points per dimension (~$2560H^{-1}$ and ~$1280H^{-1}$ for the $0.2H \times 0.2H$ and $0.4H \times 0.4H$ models, respectively). Convergence in the maximum local solid density at the saturated state for each computational domain is seen by comparing the models with the highest two resolutions. The axisymmetric filaments of solids in the low-resolution models are less efficient in collecting particles upstream and easier to become dispersed, and new filaments can sporadically form in between the existing ones, competing for solid materials. On the other hand, those in the high-resolution models are well concentrated and separated, leaving little materials in between for any more filaments to form, as exemplified by Fig. 3a. This dichotomy may be related with how well the scale height of the particle layer is resolved, which determines how many unstable modes of the linear streaming instability can operate in the simulation models.

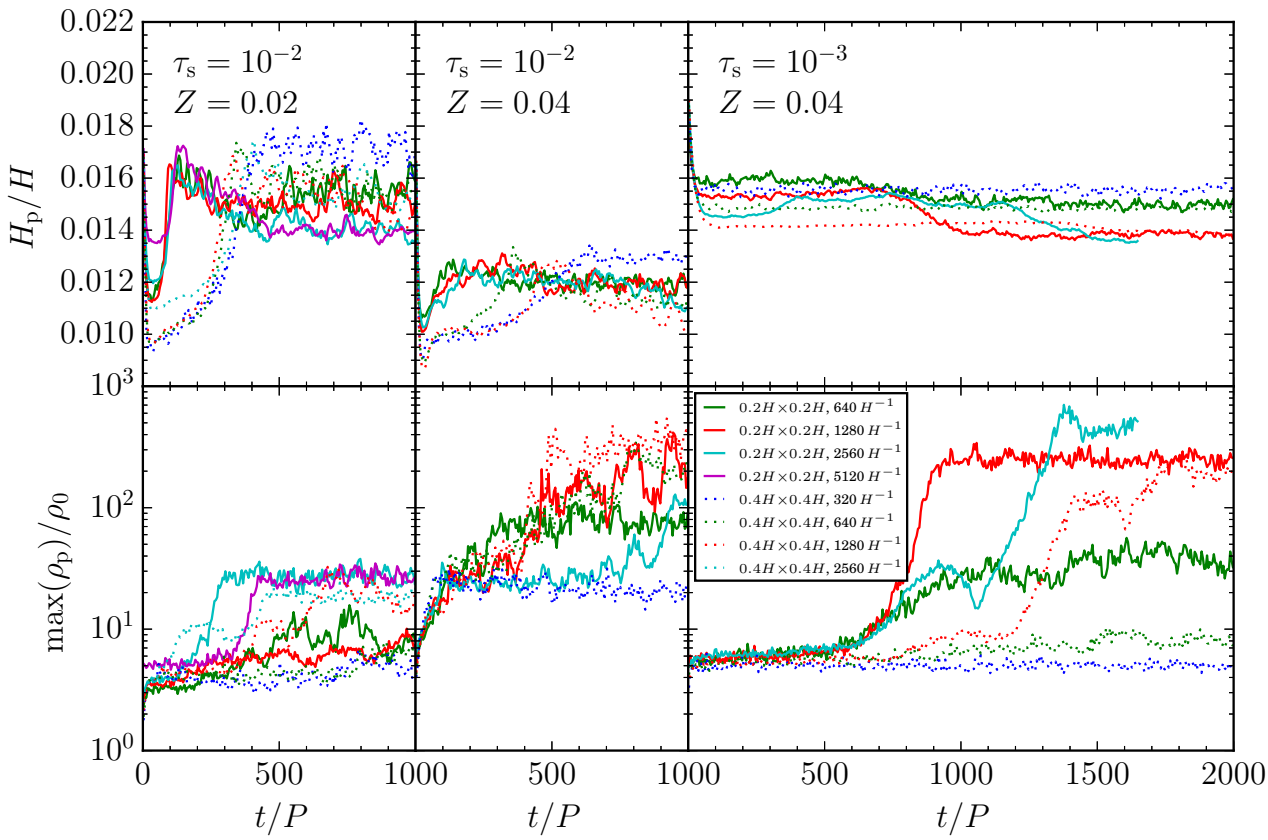

Fig. 2: Scale height of the particle layer H_p (top panels) and maximum of the local particle density ρ_p (bottom panels) as a function of time for all our 2D models that trigger strong concentration of solids at high resolutions. Each column represents one set of dimensionless stopping time τ_s and solid abundance Z. The scale height H_p, particle density ρ_p, and time t are normalized by the vertical scale height of the gas H, the initial mid-plane gas density ρ_0, and the local orbital period P, respectively. The solid and dotted lines are for a computational domain of $0.2H \times 0.2H$ and $0.4H \times 0.4H$, respectively, and the resolutions are differentiated by different colors.

Also listed in Table 2 are the estimated time to reach saturation and the final number of dominant axisymmetric solid filaments for each computational domain and resolution. There exists no obvious dependence of the saturation time on either dimensions or resolution, indicating the nonlinear and stochastic nature of the system. It depends on the contentious interaction between the first generation of filaments before a stable configuration is secured (Fig. 3). Nevertheless, we establish that the timescale for particles of $\tau_s = 10^{-2}$ to spontaneously concentrate themselves is on the order of $400P$–$950P$. Moreover, one and three major solid filaments tend to form in our $0.2H \times 0.2H$ and $0.4H \times 0.4H$ models, respectively. This is consistent with the approximate 3:2 ratio in the maximum local solid density at the saturation state and indicates that the mass budget in the solid filaments in a $0.2H \times 0.2H$ model can be overestimated (Schäfer et al. 2016). It has been shown that for $\tau_s \simeq 0.3$ particles, a model with at least $0.4H$ on each side is needed to generate consistent density distribution of solids in the saturated state of the streaming instability, where multiple solid filaments can form (Yang & Johansen 2014; R. Li et al. 2016, in preparation). Therefore, our measurement for the $0.4H \times 0.4H$ models is likely to be more accurate.

Our models demonstrate that the critical solid abundance Z_c above which spontaneous strong concentration of particles of $\tau_s = 10^{-2}$ is triggered lies in $0.01 < Z_c < 0.02$; this is a somewhat smaller value than the range $0.02 < Z_c < 0.03$ reported in Carrera et al. (2015). The reason for this discrepancy is that their models did not have enough resolution and simulation time. Carrera et al. (2015) used a 128×128 grid for a computational domain of $0.2H \times 0.2H$. With an initial solid abundance of $Z = 0.005$, they evolved the models for ~$50P$ then artificially reduced the background gas density exponentially with time so that $Z = 0.08$ was attained at $t \sim 200P$, when the simulations ended. However, as discussed above, we find that a grid of at least 512×512 with a simulation time of at least $300P$ is necessary to properly establish the saturation state of the solid concentration for particles of $\tau_s = 10^{-2}$, a condition which was not satisfied by the models of Carrera et al. (2015). We show in the next subsection that this difference in measured values of critical solid abundance is significantly more drastic for particles of $\tau_s = 10^{-3}$, which further indicates the importance of simulating small particles with high resolutions and long simulation times.

For comparison purposes, we also investigate the case of a solid abundance of $Z = 0.04$ for particles of $\tau_s = 10^{-2}$. The evolution of the particle scale height and the maximum local solid density for various resolutions and computational domains is shown in the middle panels of Fig. 2, and the properties at the saturation stage for these models are listed in Table 2. Similar to the case of $Z = 0.02$, the streaming turbulence is established for the first ~$50P$, and then the particle layer is slightly stirred up by the turbulence up to $t \sim 100P$–$200P$ for the $0.2H \times 0.2H$ models and $t \sim 400P$–$600P$ for the $0.4H \times 0.4H$ models. However, the

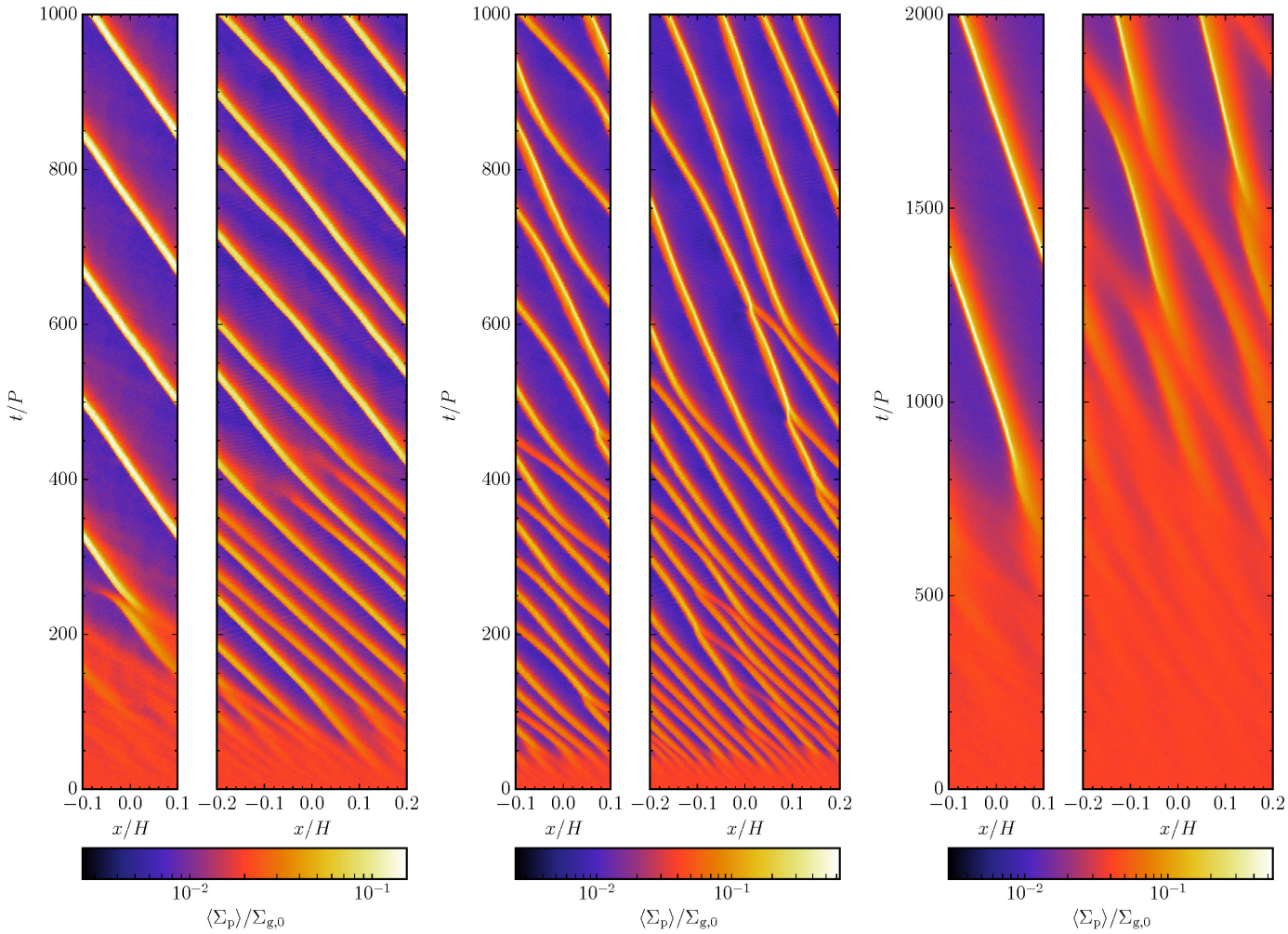

(a) $\tau_s = 10^{-2}, Z = 0.02, 2560H^{-1}$ (b) $\tau_s = 10^{-2}, Z = 0.04, 1280H^{-1}$ (c) $\tau_s = 10^{-3}, Z = 0.04, 1280H^{-1}$

Fig. 3: Evolution of the radial concentration of the particle layer for our 2D models that trigger strong concentration of solids. Three cases of different dimensionless stopping time τ_s, solid abundance Z, and model resolution are presented. The colors show the azimuthally averaged column density of the particles $\langle\Sigma_p\rangle$ as a function of radial position x and time t, where $\langle\Sigma_p\rangle$, x, and t are normalized by the initial gas column density $\Sigma_{g,0}$, the vertical scale height of the gas H, and the local orbital period P, respectively. In each case, the left and right panels are from models with a computational domain of $0.2H \times 0.2H$ and $0.4H \times 0.4H$, respectively. Note that the timespan for case (c) is twice that for cases (a) and (b).

equilibrium scale height of the particle layer is appreciably less, at a level of $\sim 0.012H$, and the corrugation mode is much less pronounced than those observed in the models for $Z = 0.02$, as shown in Fig. 1. In general, higher solid abundance gives a more sedimented layer of particles.

On the other hand, conspicuous radial concentrations of solids occur as early as $t \sim 50P$, as shown in Fig. 1, the middle panels of Fig. 2, and Fig. 3b. At this point, multiple concentrated filaments of solids with a density of a few tens of initial mid-plane gas density ρ_0 are already present, in contrast to the models for $Z = 0.02$. In the following few hundreds of orbital periods, these filaments undergo a few merging events, forming denser filaments. At the saturation stage when $t \gtrsim 500P$–$900P$, the $0.2H \times 0.2H$ models obtain a peak solid density of $\sim 100\rho_0$–$200\rho_0$ with two dense filaments, while the $0.4H \times 0.4H$ models reach $\sim 200\rho_0$–$300\rho_0$ with four dense filaments (Table 2). Therefore, more solid filaments form with higher solid abundance Z, and the concentration of solids in these filaments appear to be a super linear function of Z.

3.2. Particles of $\tau_s = 10^{-3}$

The evolution of the particle layer in our 2D models for particles of $\tau_s = 10^{-3}$ is qualitatively similar to that for particles of $\tau_s = 10^{-2}$ described in Sect. 3.1, but there exist essential quantitative differences. Figure 4 shows such an evolution for two models with solid abundance $Z = 0.03$ and $Z = 0.04$, respectively, both of which have the same computational domain of $0.2H \times 0.2H$ and resolution of $1280H^{-1}$. Similar to particles of $\tau_s = 10^{-2}$, particles of $\tau_s = 10^{-3}$ initially continue their sedimentation process until the streaming turbulence is well saturated and supporting the particle layer. Given that the sedimentation timescale for particles of $\tau_s = 10^{-3}$ is $\sim 160P$, being one order of magnitude longer than that for particles of $\tau_s = 10^{-2}$, the balance between sedimentation and turbulent excitation is not established until $t \sim 100P$–$200P$, as shown in the right panels of Fig. 2. At this point, the scale height of the particle layer is $\sim 0.015H$, somewhat higher than that for particles of $\tau_s = 10^{-2}$. We note that the largest voids of particles in the streaming tur-

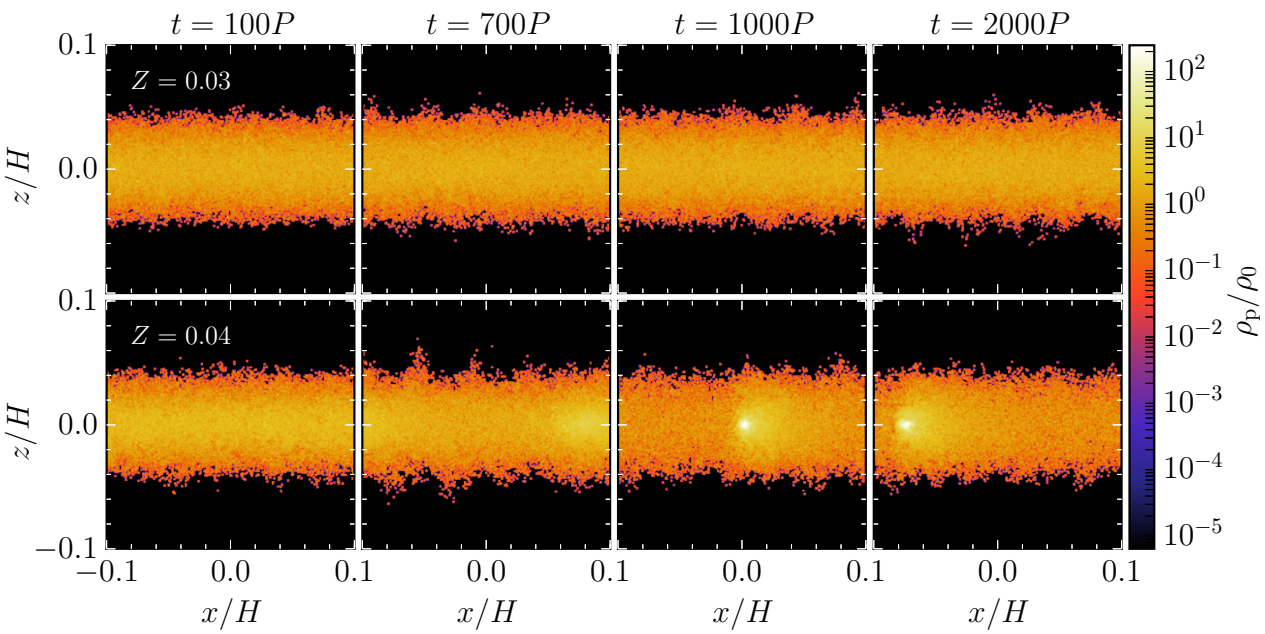

Fig. 4: Evolution of the particle density distribution for 2D models with particles of dimensionless stopping time $\tau_s = 10^{-3}$. The top and bottom panels show the models with a solid abundance of $Z = 0.03$ and $Z = 0.04$, respectively, both of which have a computational domain of $0.2H \times 0.2H$ and a resolution of $1280\,H^{-1}$. The notations and the layout are otherwise the same as those in Fig. 1.

Table 2: Saturation State of the 2D Models

Dimensions	Resolution (H^{-1})	t_{sat} (P)	N_f	$\overline{H_p}$ (H)	$\overline{\max(\rho_p)}$ (ρ_0)
(1)	(2)	(3)	(4)	(5)	(6)
$\tau_s = 10^{-2}$, $Z = 0.02$					
$0.2H \times 0.2H$	640	550	1–2	0.0155(4)	9(2)
	1280	800	1–2	0.0150(4)	7(1)
	2560	400	1	0.0141(3)	28(4)
	5120	450	1	0.0140(2)	26(3)
$0.4H \times 0.4H$	320	500	1–5	0.0172(5)	5(1)
	640	950	2–3	0.0156(2)	7(1)
	1280	800	3	0.0144(3)	18(4)
	2560	500	3	0.0153(4)	19(2)
$\tau_s = 10^{-2}$, $Z = 0.04$					
$0.2H \times 0.2H$	640	350	2	0.0120(2)	79(15)
	1280	500	2	0.0119(2)	176(73)
	2560	950	2	0.0110(1)	114(9)
$0.4H \times 0.4H$	320	600	5–6	0.0130(2)	21(3)
	640	750	4	0.0113(2)	225(45)
	1280	650	4	0.0110(4)	339(70)
$\tau_s = 10^{-3}$, $Z = 0.04$					
$0.2H \times 0.2H$	640	1000	1	0.0150(2)	34(7)
	1280	1000	1	0.0138(1)	249(28)
	2560	1500	1	0.0136(0)	453(54)
$0.4H \times 0.4H$	320	...	...	0.0155(1)	...
	640	$\gtrsim$2000	2–3	0.0147(1)	...
	1280	1900	2	0.0138(0)	193(20)

Notes. Columns: (1) Dimensions of the computational domain in terms of the gas scale height H; (2) Resolution in number of cells per H; (3) Estimated time to reach saturation in terms of the local orbital period P; (4) Number of major axisymmetric solid filaments; (5) Time-averaged scale height of the particles in H for $t > t_{sat}$; (6) Time-averaged maximum local particle density in terms of the initial mid-plane gas density ρ_0 for $t > t_{sat}$.

bulence are significantly smaller than those found in the models of particles of $\tau_s = 10^{-2}$, which is consistent with the fact that the critical wavelength of the linear streaming instability decreases with decreasing τ_s (Youdin & Goodman 2005; Youdin & Johansen 2007). The development of the corrugation of the particle layer can also be seen afterward. However, the magnitude of this effect is not as strong as that for particles of $\tau_s = 10^{-2}$. The scale height of the particles slowly increases with time and reaches its peak at $t \sim 450P$, but the resulting excitation of the particle layer is barely noticeable (Fig. 4).

We find that the particles of $\tau_s = 10^{-3}$ in the aforementioned model with solid abundance $Z = 0.04$ can strongly concentrate themselves in the mid-plane later on (Fig. 4). As shown in Fig. 3c, one axisymmetric solid filaments begins to develop at $t \sim 700P$ and increases its concentration over time. The concentration reaches its peak at $t \sim 1000P$ with a solid density of $\sim 200\rho_0$, where ρ_0 is the initial gas density in the mid-plane (Fig. 2). The filament is saturated and maintains its equilibrium state up to the end of the simulation ($t = 2000P$).

The right panels of Fig. 2 shows the evolution of the scale height and maximum local density of the particle layer for all of our 2D models with dimensionless stopping time $\tau_s = 10^{-3}$ and solid abundance $Z = 0.04$. By comparing with the other models in Fig. 2, it is evident that although particles of either size follows a similar pattern of evolution, all the timescales involved with particles of $\tau_s = 10^{-3}$ are significantly longer than those with particles of $\tau_s = 10^{-2}$. As is discussed above, these include the timescales for the initial balance between sedimentation and streaming turbulence to establish, for the corrugation mode to develop, and for the radial concentration of the particles in the mid-plane to reach saturation, the last of which requires more than $1000P$. We note also that in contrast to particles of $\tau_s = 10^{-2}$, the initial scale height of the particles of $\tau_s = 10^{-3}$ slightly decreases with increasing resolution.

Table 2 lists the time-averaged properties of the particle layer at the final saturation stage for all of our 2D models. Similar to particles of $\tau_s = 10^{-2}$, there exists a critical resolution above which strong concentration of particles of $\tau_s = 10^{-3}$ occurs; this resolution is $\sim 1280H^{-1}$ for both $0.2H \times 0.2H$ and $0.4H \times 0.4H$ models. We observe that the timescale for particles of $\tau_s = 10^{-3}$

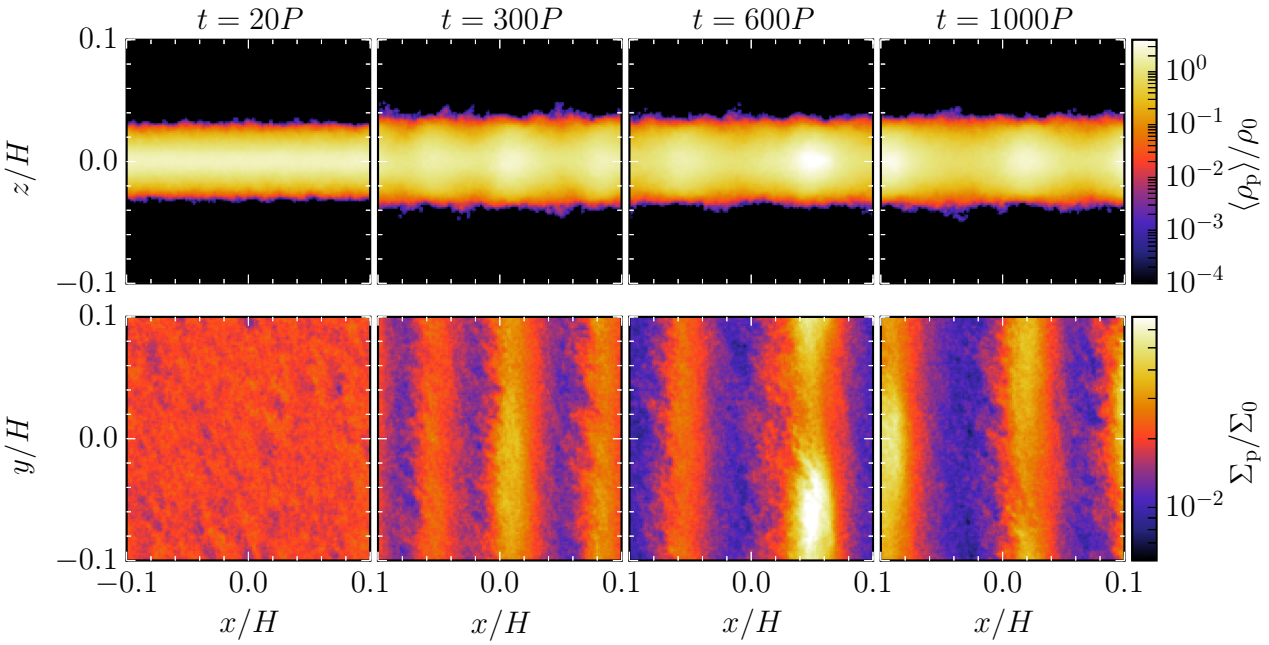

Fig. 5: Side and top views of the particle layer for a 3D model with particles of $\tau_s = 10^{-2}$ and a solid abundance of $Z = 0.02$. The time t in terms of the local orbital period P increases from left to right. The top panels show the azimuthal average of the particle density ρ_p with respect to the initial gas density in the mid-plane ρ_0, while the bottom panels show the column density of solids Σ_p with respect to the initial column density of gas Σ_0. The coordinates are normalized by the vertical scale height of the gas H. The model has a computational domain of $0.2H$ on each side and a resolution of $640H^{-1}$.

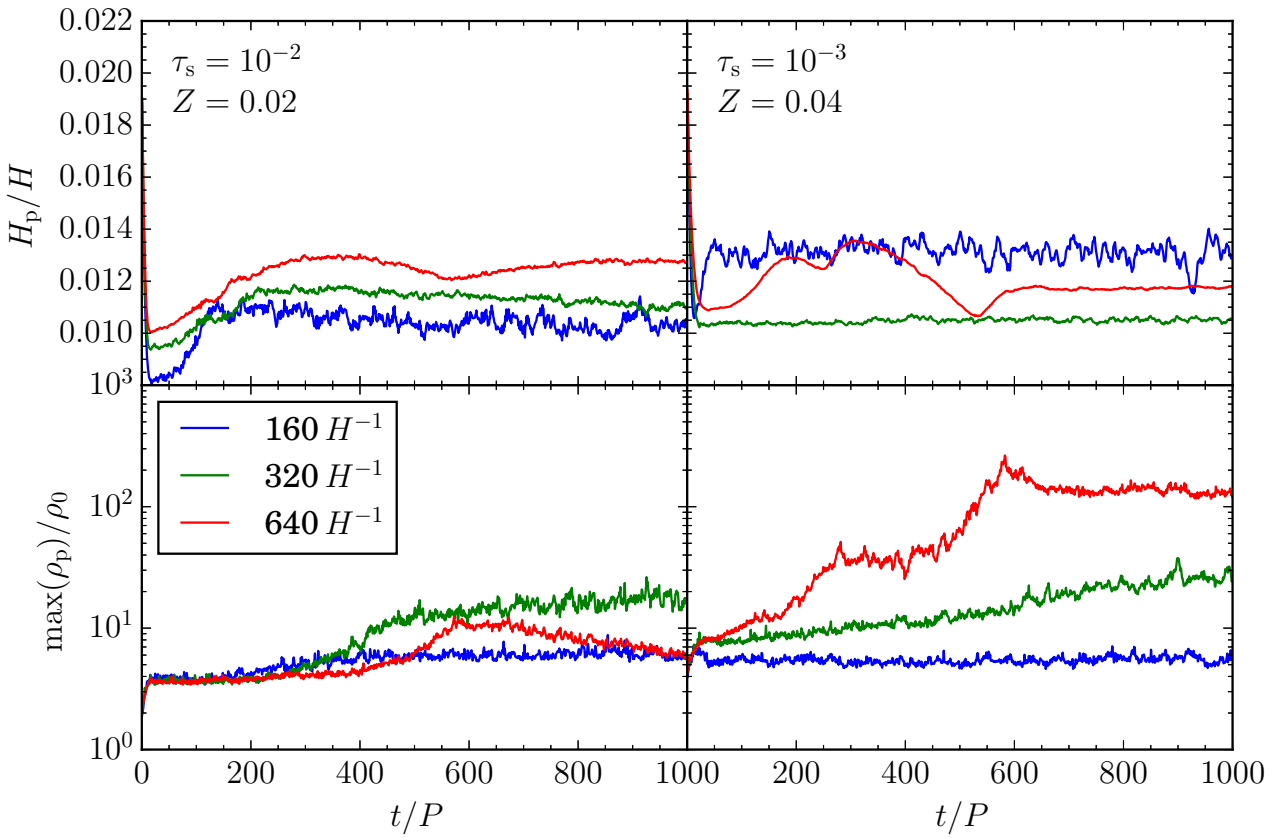

Fig. 6: Scale height of the particle layer H_p (top panels) and maximum of the local particle density ρ_p (bottom panels) as a function of time for all our 3D models. Each column represents one set of dimensionless stopping time τ_s and solid abundance Z. All the models have a computational domain of $0.2H$ on each side. Different line colors represent different resolutions.

to spontaneously concentrate themselves into dense axisymmetric filaments is on the order of $1000P$–$2000P$. One and two major solid filaments tend to form in our $0.2H \times 0.2H$ and $0.4H \times 0.4H$ models, respectively. The maximum local solid density in these filaments can be as high as $200\rho_0$–$600\rho_0$. This is one order of magnitude higher than what is achieved by particles of $\tau_s = 10^{-2}$ with an abundance of $Z = 0.02$. It becomes comparable when either type of particles has $Z = 0.04$, but the former has relatively stronger concentration due to smaller number of filaments formed. Finally, the scale height of the particles in these models are also noticeably reduced when strong concentration occurs, which is due to further sedimentation of particles in the dense filaments.

Our models indicate that the critical solid abundance Z_c to trigger strong concentration of particles of $\tau_s = 10^{-3}$ lies in $0.03 < Z_c < 0.04$. By contrast, Carrera et al. (2015) did not find any sign of significant concentration for solid abundances up to $Z \sim 0.2$. It should be clear by now that the reason for this discrepancy is due to the long timescale ($\gtrsim 1000P$) and high model resolution ($\gtrsim 1280H^{-1}$) required to realize the process. The 2D models in Carrera et al. (2015) had a resolution of $640H^{-1}$ and a simulation time of $\sim 200P$. As shown in Fig. 2, only an equilibrated streaming turbulence can be observed during this period. Before discussing the implications of our findings for planetesimal formation scenarios, we further investigate the effect of the azimuthal dimension using 3D models in the next section.

4. Three-dimensional models

In this section, we use 3D models to study the effect of the azimuthal dimension on the spontaneous concentration of small solid particles. We focus on a computational domain of 0.2 times gas scale height H on each side and a solid abundance that can trigger significant solid concentration in the 2D models reported in Sect. 3. Note that Johansen & Youdin (2007) found that the morphological features of the streaming turbulence for tightly coupled particles in unstratified models are not axisymmetric, which can lead to stronger density fluctuations. By comparing each 3D model with its 2D counterpart, we find how the azimuthal dimension can change the properties of a strictly axisymmetric distribution of sedimented solids.

4.1. Particles of $\tau_s = 10^{-2}$

Figure 5 shows the evolution of the particle layer for particles of dimensionless stopping time $\tau_s = 10^{-2}$ and a solid abundance of $Z = 0.02$, at a resolution of $640H^{-1}$. Similar to its 2D counterpart, the particles obtain their balance between sedimentation and streaming turbulence within $\sim 20P$, where P is the local orbital period, as also shown in the left panels of Fig. 6. The resulting scale height of particles is $\sim 0.010H$, slightly lower than that in the 2D model. From the top view of the particle disk, it can be seen that the streaming turbulence is indeed non-axisymmetric, with small-scale filamentary structures driven by background Keplerian shear. This is consistent with what was found in unstratified models for tightly coupled particles (Johansen & Youdin 2007). From $t \sim 20P$ to $\sim 200P$, the particles are gradually excited in the vertical direction, and the scale height slightly increases to the level of $\sim 0.012H$. In contrast to the corrugation mode found in 2D models, however, the excitation of the particles in the 3D models is not regular in the radial direction, and the level of the excitation is appreciably less.

In the meantime, multiple radial concentrations of solids near the mid-plane begin to appear, as shown in Figs. 5 and 7. As the

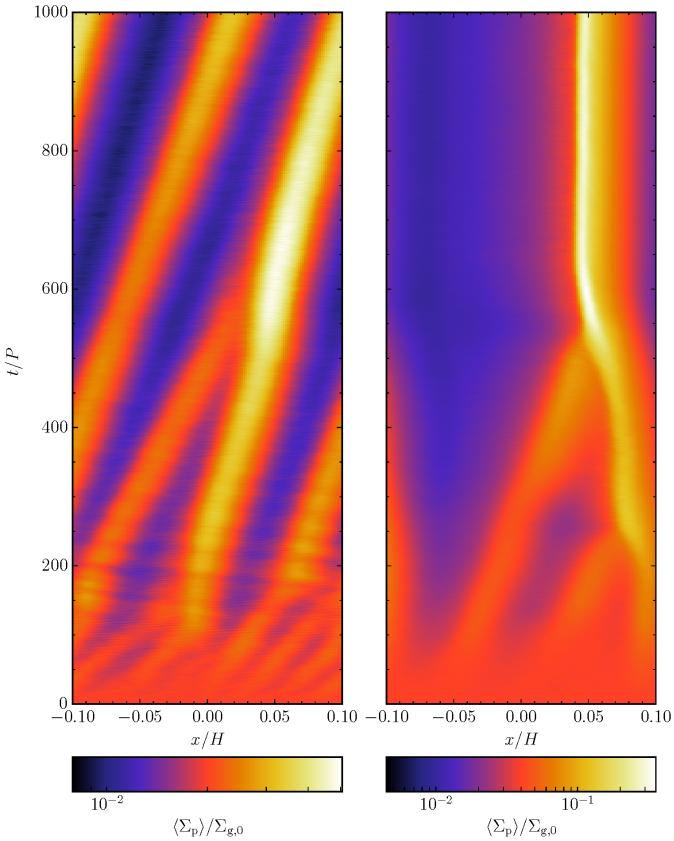

Fig. 7: Evolution of the radial concentration of the particle layer for two 3D models. The colors show the azimuthal average of the column density of the particles Σ_p as a function of radial position x and time t, where Σ_p, x, and t are normalized by the initial gas column density $\Sigma_{g,0}$, the vertical scale height of the gas H, and the local orbital period P, respectively. The left panel has particles of dimensionless stopping time $\tau_s = 10^{-2}$ and a solid abundance of $Z = 0.02$, while the right panel has $\tau_s = 10^{-3}$ and $Z = 0.04$. Both models have the same computational domain of $0.2H$ on each side and resolution of $640H^{-1}$.

solids continue to accumulate, the filamentary structures become more and more aligned in the azimuthal direction. Interestingly, though, these axisymmetric filaments migrate radially outwards, contrary to what is seen in the 2D models. Similar behavior was also seen in the 3D models conducted by Carrera et al. (2015), who used an explicit method to integrate the mutual drag force. We find that even though the average radial velocity of all particles remains negative, a significant fraction of particles in and near these filaments indeed have positive radial velocity, however distributed in a non-axisymmetric fashion. Nevertheless, the maximum local density of solids in these filaments reaches ~ 10 times the initial gas density in the mid-plane ρ_0 at $t \sim 600P$ (Fig. 6), a similar level and timescale observed in the 2D model of the same resolution and dimensions (Fig. 2). At the end of the simulation when $t = 1000P$, the system has not obtained a statistically steady state yet. Note also that the resolution we have achieved here remains lower than the critical resolution required to trigger significant concentration in the corresponding 2D models (Sect. 3.1).

Also shown in the left panels of Fig. 6 are the evolution of the scale height of the particle layer and the maximum local solid density for otherwise the same models but with two lower reso-

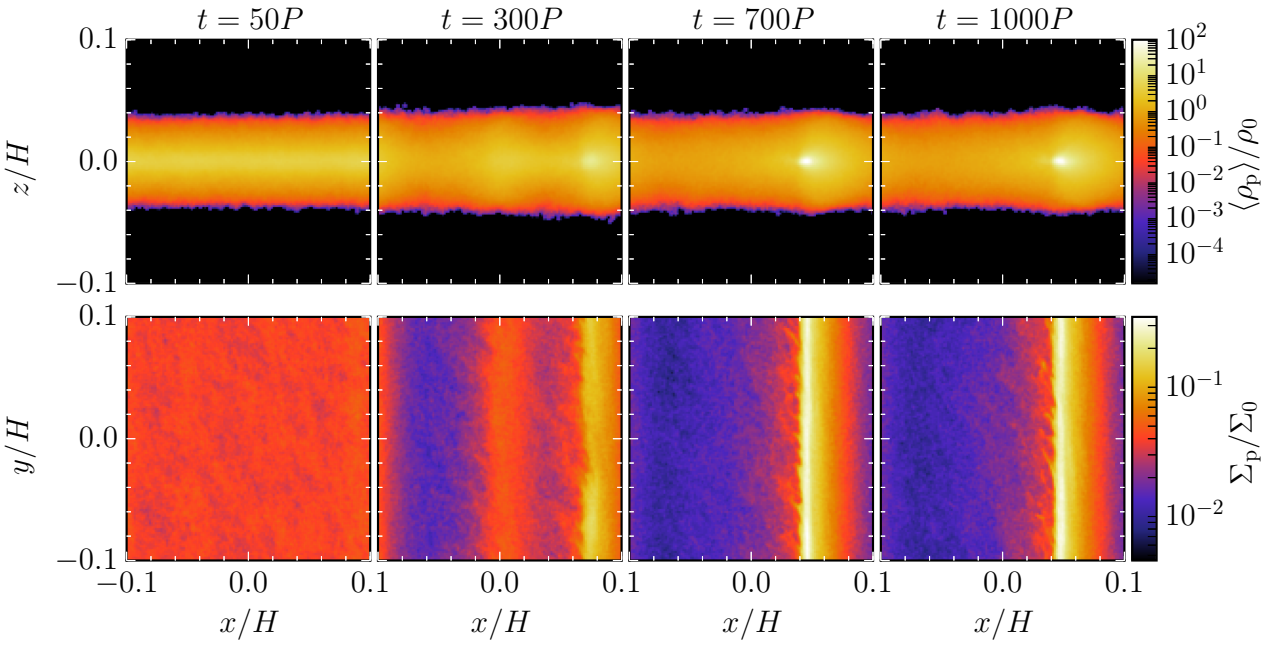

Fig. 8: Side and top views of the particle layer for a 3D model with particles of $\tau_s = 10^{-3}$ and a solid abundance of $Z = 0.04$. The notations, layout, and model specification are otherwise the same as those in Fig. 5.

lutions. Similar to the trend found in the 2D models for particles of $\tau_s = 10^{-2}$ (Sect. 3.1), the equilibrium scale height increases slightly with increasing resolution at $t \sim 20P$, and all the models undergo moderate vertical excitation of particles during $t \sim 20P$ to $\sim 150P$. The two lower-resolution models, however, only drive one axisymmetric filamentary concentration of particles during $t \sim 200P$ to $1000P$. Because of this, the model with a resolution of $320H^{-1}$ reaches a higher local solid density of $\sim 20\rho_0$ in the filament than the model with a resolution of $640H^{-1}$. It remains to be investigated whether a convergent saturation state can be achieved with even higher-resolution models.

4.2. Particles of $\tau_s = 10^{-3}$

Figure 8 shows the evolution of the particle layer for particles of dimensionless stopping time $\tau_s = 10^{-3}$ and a solid abundance of $Z = 0.04$, at a resolution of $640H^{-1}$. Similar to its 2D counterpart at the same resolution, the balance between sedimentation and streaming turbulence is attained at $t \sim 50P$, as also shown in the right panels of Fig. 6. The scale height of the particle layer at this point, though, is $\sim 0.011H$, which is appreciably less than $\sim 0.016H$ maintained by the 2D model. Nevertheless, the particles are gradually excited to a level of scale height $\sim 0.013H$ over the period of $50P \lesssim t \lesssim 200P$.

As shown in the right panel of Fig. 7 as well as Fig. 8, three axisymmetric filaments of solids begin to develop at $t \sim 100P$. Similar to the 3D model for particles of $\tau_s = 10^{-2}$ at the same resolution of $640H^{-1}$ (Sect. 4.1), two of the three filaments migrate outwards. They eventually merge with the third at $t \sim 250P$ and $t \sim 550P$, respectively. As a result, the merged filament of solids becomes so dense that it virtually stops any further radial drift, and maintain its state up to the end of the simulation at $t = 1000P$. The maximum local solid density reaches the order of $10^2\rho_0$ and the average scale height of the particles slightly decreases due to further sedimentation in the dense filaments, as shown in the right panels of Fig. 6. This concentration of solids is at the same level of what is obtained by the corresponding 2D models, albeit at a lower resolution than the critical one required by the latter (Sect. 3.2).

The right panels of Fig. 6 shows the scale height of the particle layer and the maximum local solid density as a function of time for our 3D models with particles of $\tau_s = 10^{-3}$ and $Z = 0.04$ at three different resolutions. The model with the resolution of $160H^{-1}$ does not show any sign of significant concentration of solids over the course of the simulation. At the resolution of $320H^{-1}$, accumulation of solids into one broad filament appears, and the density of the filament gradually and steadily increases with time, reaching $\sim 30\rho_0$ at $t = 1000P$. As discussed above, the model with the highest resolution of $640H^{-1}$ shows strong concentration of solids and the system reaches its final saturated state at $t \sim 650P$, which is considerably less than the timescale of $\sim 1000P$ required by its 2D counterpart (Fig. 2 and Table 2).

5. Implications for planetesimal formation

The 2D and 3D models we present in Sects. 3 and 4 indicate that significant spontaneous concentration of solids in protoplanetary disks can occur at a considerably less solid abundance than reported in Carrera et al. (2015), especially for particles as small as $\tau_s = 10^{-3}$. It is a matter of timescale and resolution for the process to operate. For particles of $\tau_s = 10^{-2}$ and those of $\tau_s = 10^{-3}$, we identify that timescales of $400P$–$1000P$ and $600P$–$2000P$ are required, respectively. We note that even though a considerably longer timescale is necessary for small particles to concentrate themselves, their radial drift timescale is also proportionately longer due to their small stopping times. The radial-drift timescale is given by (Adachi et al. 1976):

$$t_{\rm drift} = \left(\frac{1+\tau_s^2}{4\pi\Pi\tau_s}\right)\left(\frac{H}{R}\right)^{-1} P \quad (1)$$

$$\simeq 3\times 10^4 \left(\frac{\tau_s}{10^{-3}}\right)^{-1}\left(\frac{\Pi}{0.05}\right)^{-1}\left(\frac{H/R}{0.05}\right)^{-1} P, \quad (2)$$

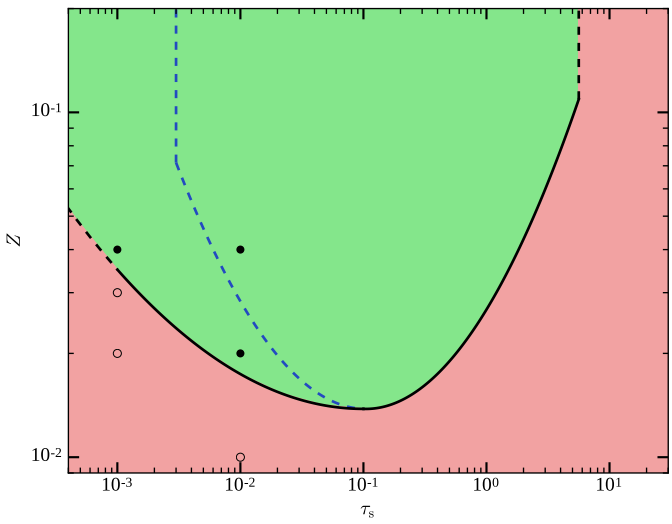

Fig. 9: Revised critical solid abundance as a function of the dimensionless stopping time τ_s from Carrera et al. (2015). The filled and open circles show our models with and without significant radial concentration of solids, respectively. The solid black line for $\tau_s \gtrsim 10^{-1}$ and the dashed blue line for $\tau_s \lesssim 10^{-1}$ are the unmodified critical curve from Carrera et al. (2015). The black solid line for $\tau_s \lesssim 10^{-1}$ shows the revised part of the critical curve, where the black dashed line is the extrapolation of it. For solid abundances Z above the black line (green region), spontaneous concentration of solid particles by the streaming instability can occur.

for $\tau_s \ll 1$, where $\Pi \equiv \Delta v/c_s$ and Δv is the reduction in gas velocity due to radial pressure gradient. The timescales for $\tau_s = 10^{-2}$ and $\tau_s = 10^{-3}$ are thus one order of magnitude longer than those required for driving radial concentration of solids by the streaming turbulence. Therefore, these small particles do not suffer from the radial drift barrier any worse than large particles. Moreover, the radial drift barrier is further alleviated once significant concentration of solids is established due to the back reaction of the drag force from the solids to the gas (Nakagawa et al. 1986; Johansen & Youdin 2007).

Given our findings of a much reduced critical solid abundance Z_c for which particles of $\tau_s \ll 1$ can spontaneously concentrate themselves, we hereby revise the Z_c curve as a function of τ_s reported in Carrera et al. (2015). The critical curve for $\tau_s \gtrsim 0.1$ is the same as in Carrera et al. (2015) and given by

$$\log Z_c = 0.3(\log \tau_s)^2 + 0.59 \log \tau_s - 1.57 \quad (\tau_s > 0.1), \tag{3}$$

where log is the logarithm with base 10. On the other hand, we arbitrarily choose a quadratic function of $\log \tau_s$ for $\log Z_c$ such that it passes $Z_c = 0.035$ at $\tau_s = 10^{-3}$ and smoothly join the other curve at $\tau_s = 0.1$ with a slope of zero. The resulting function is given by

$$\log Z_c = 0.10(\log \tau_s)^2 + 0.20 \log \tau_s - 1.76 \quad (\tau_s < 0.1). \tag{4}$$

The updated critical curve is shown in Fig. 9.

Moreover, we note that even though particles of $\tau_s = 10^{-2}$ can concentrate at a lower solid abundance of $Z = 0.02$, their concentration is one order of magnitude less dense than particles of $\tau_s = 10^{-3}$ at $Z = 0.04$. The maximum local solid density reached by particles of $\tau_s = 10^{-3}$ is about 200–600 times the background gas density in the mid-plane ρ_0, while that by particles of $\tau_s = 10^{-2}$ is only about $20\rho_0$–$30\rho_0$. By comparing $Z = 0.02$ and $Z = 0.04$ for particles of $\tau_s = 10^{-2}$ (Sect. 3.1), we note also that with only a difference of twice the solid abundance, the response of the saturated state for particles of $\tau_s = 10^{-2}$ can be more than one order of magnitude stronger. At $Z = 0.04$, they reach a peak density of $\sim 100\rho_0$–$300\rho_0$, on the same order of that by particles of $\tau_s = 10^{-3}$. However, due to the formation of relatively more dense filaments of solids at smaller separations for particles of $\tau_s = 10^{-2}$, the saturated peak density remains comparatively lower than that of particles of $\tau_s = 10^{-3}$.

This observation leads to an interesting scenario for planetesimal formation. Solid particles of smaller sizes might be more predisposed towards gravitational collapse inside self-induced dense filaments of solids than those of larger sizes. To see this, the Roche density ρ_R is given by

$$\frac{\rho_R}{\rho_0} = \frac{9M_\star}{4\pi a^3 \rho_0} \tag{5}$$

$$= 240 \left(\frac{M_\star}{M_\odot}\right)\left(\frac{a}{2.5\ \mathrm{au}}\right)^{-3}\left(\frac{\rho_0}{10^{-10}\ \mathrm{g\ cm^{-3}}}\right)^{-1}, \tag{6}$$

where $M_\star$ and a are the mass of and the distance to the central star, respectively, and ρ_0 is the gas density in the mid-plane. The normalization is applied at the location of the Asteroid Belt in the MMSN. Note that the observed gas densities in the terrestrial region of a young protoplanetary disk can be one or two magnitudes higher (see, e.g., Dutrey et al. 2014, and references therein), and a gas density of 10^{-8}–10^{-10} g cm^{-3} for $a < 5$ au can also be seen in numerical simulations of star-irradiated accretion disk models at their earliest evolution stages (Bitsch et al. 2015; Baillié et al. 2016). In any case, the solid concentration achieved in our models with particles of $\tau_s = 10^{-3}$ is well above the Roche density in the terrestrial region of a wide range of disks when the solid abundance $Z \sim 0.04$, while it may require particularly dense disks or further outward locations for particles of $\tau_s = 10^{-2}$ to drive planetesimal formation unless $Z \gtrsim 0.04$ also. Most importantly, we have demonstrated that inside the ice line, strong concentration of mm-sized particles, whose growth is limited by bouncing and fragmentation (Zsom et al. 2010; Birnstiel et al. 2012), and hence planetesimal formation therein is possible, bridging the problematic gap between dust coagulation and planetesimal formation (Drążkowska & Dullemond 2014).

Finally, several open questions remain in concentrating small particles by the streaming instability. We have observed further sedimentation in dense filaments in our models, indicating that the velocity dispersion of the particles decreases in the dense regions. It remains to be seen if further dust growth could proceed inside such an environment, given the reduced relative velocities, and if the dust growth in turn could drive more spontaneous concentration of solid materials via the streaming instability. Moreover, the presence of the magnetic fields could render rich structure in the gaseous protoplanetary disks, and the disk mid-plane can be turbulent with various strengths at different locations (Turner et al. 2014), which significantly affects the ability of solid materials to sediment onto the mid-plane (e.g., Okuzumi & Hirose 2011; Zhu et al. 2015). This has nontrivial effects on the dust coagulation and the radial concentration of solids for planetesimal formation to occur (Johansen et al. 2014; Testi et al. 2014).

6. Summary

In this work, we revisit the condition for the spontaneous concentration of solid particles driven by the streaming instability in

the regime of dimensionless stopping time $\tau_s \ll 1$, as originally investigated by Carrera et al. (2015). Using the local-shearing-box approximation, we simulate a sedimented layer of solid particles of same size in a laminar gaseous environment, developing streaming turbulence and possibly the ensuing radial concentration of particles. With the assistance of the numerical algorithm for the stiff mutual drag force by Yang & Johansen (2016), we are able to conduct the same simulation models of Carrera et al. (2015) with significantly higher resolutions and longer simulation times. We focus on two stopping times $\tau_s = 10^{-2}$ and 10^{-3}, and systematically vary the solid-to-gas column density ratio Z and the resolution, with two computational domains of $0.2H \times 0.2H$ and $0.4H \times 0.4H$ in the radial-vertical plane, where H is the local scale height of the gas. We also conduct a few 3D counterparts of the same models and find similar results.

We find that small solid particles can indeed spontaneously concentrate themselves into high density via the streaming instability, given enough time and resolution. For particles of $\tau_s = 10^{-2}$ and 10^{-3}, the critical solid abundance Z_c above which strong concentration of solids occurs is in the range of $0.01 < Z_c < 0.02$ and $0.03 < Z_c < 0.04$, respectively. The timescales required for this process to reach saturation are approximately $400P$–$1000P$ and $600P$–$2000P$, respectively, where P is the local orbital period. For $\tau_s = 10^{-2}$ at a solid abundance of $Z = 0.02$, a maximum local solid density of $20\rho_0$–$30\rho_0$ is observed, where ρ_0 is the initial mid-plane density of the gas, while for $\tau_s = 10^{-3}$ at a solid abundance of $Z = 0.04$, that of $200\rho_0$–$600\rho_0$ results. We also find a super-linear dependence of the solid concentration on the solid abundance. With these new measurements, we hereby revise the critical solid abundance curve of Carrera et al. (2015) in the regime of $\tau_s \ll 1$ in Fig. 9. For a solid density of $\gtrsim 10^2\rho_0$, direct gravitational collapse of mm-sized particles can occur and form planetesimals in the terrestrial region of typical protoplanetary disks, as long as the solid abundance reaches the level of a few percent. This may help alleviate the problematic size gap between the largest particles from dust coagulation and the smallest particles that can spontaneously concentrate themselves via the streaming instability, especially inside the ice line of a protoplanetary disk.

Acknowledgements. All the simulation models presented in this work were performed on resources provided by the Swedish National Infrastructure for Computing (SNIC) at PDC Center for High Performance Computing in KTH Royal Institute of Technology and at Lunarc in Lund University, both of which are located in Sweden. This research was supported by the European Research Council under ERC Starting Grant agreement 278675-PEBBLE2PLANET. A.J. is grateful for financial support from the Knut and Alice Wallenberg Foundation and from the Swedish Research Council (grant 2010-3710).

References

Adachi, I., Hayashi, C., & Nakazawa, K. 1976, Progress of Theoretical Physics, 56, 1756
Bai, X.-N. & Stone, J. M. 2010a, ApJ, 722, 1437
Bai, X.-N. & Stone, J. M. 2010b, ApJS, 190, 297
Bai, X.-N. & Stone, J. M. 2014, ApJ, 796, 31
Baillié, K., Charnoz, S., & Pantin, E. 2016, A&A, 590, A60
Barge, P. & Sommeria, J. 1995, A&A, 295, L1
Baruteau, C., Crida, A., Paardekooper, S.-J., et al. 2014, in Protostars and Planets VI, ed. T. Montmerle, D. Ehrenreich, & A.-M. Lagrange (Univ. Arizona Press, Tucson, AZ), 667–689
Birnstiel, T., Klahr, H., & Ercolano, B. 2012, A&A, 539, A148
Bitsch, B., Johansen, A., Lambrechts, M., & Morbidelli, A. 2015, A&A, 575, A28
Brandenburg, A. & Dobler, W. 2002, Computer Physics Communications, 147, 471
Brandenburg, A., Nordlund, A., Stein, R. F., & Torkelsson, U. 1995, ApJ, 446, 741
Brauer, F., Dullemond, C. P., Johansen, A., et al. 2007, A&A, 469, 1169
Carrera, D., Johansen, A., & Davies, M. B. 2015, A&A, 579, A43
Drążkowska, J. & Dullemond, C. P. 2014, A&A, 572, A78
Dutrey, A., Semenov, D., Chapillon, E., et al. 2014, in Protostars and Planets VI, ed. T. Montmerle, D. Ehrenreich, & A.-M. Lagrange (Univ. Arizona Press, Tucson, AZ), 317–338
Goldreich, P. & Lynden-Bell, D. 1965, MNRAS, 130, 125
Haisch, Jr., K. E., Lada, E. A., & Lada, C. J. 2001, ApJ, 553, L153
Hawley, J. F., Gammie, C. F., & Balbus, S. A. 1995, ApJ, 440, 742
Hayashi, C. 1981, Progress of Theoretical Physics Supplement, 70, 35
Hockney, R. W. & Eastwood, J. W. 1988, Computer Simulation Using Particles (CRC Press, New York, NY)
Johansen, A., Blum, J., Tanaka, H., et al. 2014, in Protostars and Planets VI, ed. T. Montmerle, D. Ehrenreich, & A.-M. Lagrange (Univ. Arizona Press, Tucson, AZ), 547–570
Johansen, A., Mac Low, M.-M., Lacerda, P., & Bizzarro, M. 2015, Science Advances, 1, 1500109
Johansen, A. & Youdin, A. 2007, ApJ, 662, 627
Johansen, A., Youdin, A., & Klahr, H. 2009a, ApJ, 697, 1269
Johansen, A., Youdin, A., & Mac Low, M.-M. 2009b, ApJ, 704, L75
Johansen, A., Youdin, A. N., & Lithwick, Y. 2012, A&A, 537, A125
Kataoka, A., Tanaka, H., Okuzumi, S., & Wada, K. 2013, A&A, 557, L4
Klahr, H. & Hubbard, A. 2014, ApJ, 788, 21
Lorén-Aguilar, P. & Bate, M. R. 2015, MNRAS, 453, L78
Lyra, W. 2014, ApJ, 789, 77
Mamajek, E. E. 2009, in American Institute of Physics Conference Series, Vol. 1158, American Institute of Physics Conference Series, ed. T. Usuda, M. Tamura, & M. Ishii, 3–10
Nakagawa, Y., Sekiya, M., & Hayashi, C. 1986, Icarus, 67, 375
Okuzumi, S. & Hirose, S. 2011, ApJ, 742, 65
Papaloizou, J. C. B. & Terquem, C. 2006, Reports on Progress in Physics, 69, 119
Safronov, V. S. 1969, Evoliutsiia doplanetnogo oblaka. (Nauka, Moscow)
Schäfer, U., Yang, C.-C., & Johansen, A. 2016, A&A, in press [arXiv: 1611.02285]
Simon, J. B., Armitage, P. J., Li, R., & Youdin, A. N. 2016, ApJ, 822, 55
Testi, L., Birnstiel, T., Ricci, L., et al. 2014, in Protostars and Planets VI, ed. T. Montmerle, D. Ehrenreich, & A.-M. Lagrange (Univ. Arizona Press, Tucson, AZ), 339–361
Turner, N. J., Fromang, S., Gammie, C., et al. 2014, in Protostars and Planets VI, ed. T. Montmerle, D. Ehrenreich, & A.-M. Lagrange (Univ. Arizona Press, Tucson, AZ), 411–432
Weidenschilling, S. J. 1977a, MNRAS, 180, 57
Weidenschilling, S. J. 1977b, Ap&SS, 51, 153
Whipple, F. L. 1972, in Twenty-First Nobel Symposium, From Plasma to Planet, ed. A. Elvius (Wiley Interscience Division, New York, NY), 211
Yang, C.-C. & Johansen, A. 2014, ApJ, 792, 86
Yang, C.-C. & Johansen, A. 2016, ApJS, 224, 39
Yang, C.-C. & Krumholz, M. 2012, ApJ, 758, 48
Youdin, A. & Johansen, A. 2007, ApJ, 662, 613
Youdin, A. N. 2010, in EAS Publications Series, Vol. 41, Physics and Astrophysics of Planetary Systems, ed. T. Montmerle, D. Ehrenreich, & A.-M. Lagrange (EDP, Les Ulis), 187–207
Youdin, A. N. & Goodman, J. 2005, ApJ, 620, 459
Zhu, Z., Stone, J. M., & Bai, X.-N. 2015, ApJ, 801, 81
Zsom, A., Ormel, C. W., Güttler, C., Blum, J., & Dullemond, C. P. 2010, A&A, 513, A57